# Toward Continuous Nano-Plastic Monitoring in Water by High Frequency Impedance Measurement With Nano-Electrode Arrays

Daniele Goldoni, *Graduate Student Member, IEEE*, Luigi Rovati, *Member, IEEE*, and Luca Selmi, *Fellow, IEEE*

Abstract—We explore the potentiality of high frequency impedance measurements with CMOS nano-electrode (NE) arrays for nano-plastic pollutant particles monitoring in water. This technology offers benefits as nano-scale resolution, high parallelization, scalability, label-free single particle detection, and automatic measurements without operator intervention. Simple models are proposed for size and concentration estimation. The former integrates measurements of adjacent electrodes and shows uncertainty comparable to the nominal one with mean prediction error lower than 45% down to 50 nm radius. The latter accounts for noise in the definition of the sensing volume. We report a worst case concentration error lower than a factor 1.7 under stationary and continuous flow, which demonstrates the potential of this technology for automated measurements.

Index Terms—CMOS nanoelectrode arrays, environmental sensor, high-frequency impedance measurements, label-free pollutant detection, microplastic, nanoplastic, single particle detection, sub-micrometer particle sizing, water monitoring.
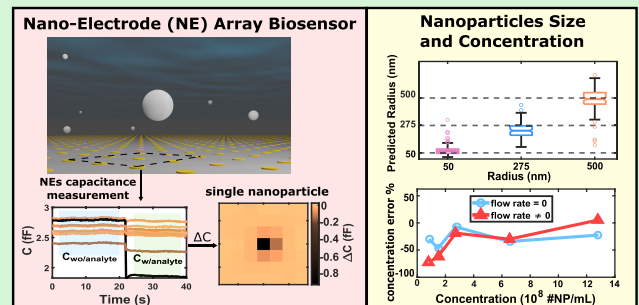
I. INTRODUCTION

WATER pollution threatens water quality and availability, both being critical for the health of humans, animals, and the environment [1]. Besides highly toxic heavy metals [2], micro- and nano-plastic pollutants are causing growing concerns [3], since they have already been found in drinking water [4], [5] and human blood [6]. Detailed knowledge of the exposure pathways and toxic effects is still lacking, particularly for nanoscale pollutants [7], [8], [9], [10], [11]. Consequently, there is a growing need for monitoring systems that generate real-time quantitative data and alerts of nanopollutant spreading in all contexts, from tap water to freshwater sources (e.g., river, lake, and sea), and even biological samples [6].

The ionic strength of water varies widely depending on the source and the location on earth, depth, ground composition, temperature, and nearby human activity [12]. The average salinity of water can vary from essentially zero in pure water to 0.05% for tap water and freshwater ($\approx$10 mM), 0.05% to 3% for brackish water, up to 3.5% for seawater ($\approx$500 mM) [12]. In spite of increasing research efforts and the World Health Organization (WHO) calling for more attention to micro- and nano-plastic pollution in water [13], neither well-defined standards on sampling, detection and measurement techniques have yet been defined [4], [10], [14], [15], nor consensus has been reached for plastic pollutant nomenclature based on size [16], [17].

In this context, current analytical technologies for monitoring pollutants in water are mainly based on optical microscopy and vibrational spectroscopy, which are bulky, expensive, time-consuming, and require complex sampling procedures carried out by skilled operators [4], [15]. In particular, Fourier transform infrared spectroscopy (FT-IR) and Raman spectroscopy have limitations in detecting particles smaller than 1 μm diameter [10], [15], thus preventing their use for *nano*-plastics monitoring [4], [10], [11], [15]. A shortlist of techniques recently proposed to overcome these limitations is given in Table I. Systems based on optical

TABLE I
RECENTLY PUBLISHED MEASUREMENT TECHNIQUES FOR CONTINUOUS POLLUTANTS MONITORING IN WATER

Ref.	Measurement Principle	Pollutant Type	Size Estimation	Concentration Estimation	Continuous Measurement	Single Particle Detection	Material Classification
[18]	EIS[a] and ML	Large Microplastics	✓[b]	✓	✓	✗	✓
[19]	BLGR and ML	Metals	✗	✓	✓	✗	✓[c]
[20]	RMS	Microplastic	✗	✓	✓	✗	✗
[21]	Potentiostat with SPE	Metals	✗	✓	✓	✗	✓
[22]	DLS	Nanoparticles	✓	✗	✓	✗	✗
This work	HFIS NE array	Metals, nanoplastics	✓	✓	✓	✓	✓[d]

EIS: Electrochemical Impedance Spectroscopy, ML: Machine Learning, BLGR: Block Loop-Gain Resonator. SPE: Single Planar Electrode. RMS: Resonance Microwave Spectroscopy. DLS: Dynamic Light Scattering.
a: 20 Hz - 2 MHz frequency range. b: range 2 mm - 4 mm. c: Na^+, K^+, and Mg^{2+} ions. d: discussed in Section IV.

methods [23], [24], [25], radio frequency resonators [26], [27], and electrochemical impedance spectroscopy (EIS) [28] (sometimes integrating computer vision technology [29], [30]), have been published as well. EIS was also proposed for real-time monitoring of pollutants in graphene filters [31], and capacitive measurement for particle detection in lubricating oil [32]. High frequency impedance spectroscopy (HFIS) with nano-electrodes (NEs) array [33], [34], [35], [36] is a still largely unexplored (bio)sensing technology, with demonstrated capability to directly detect by purely electrical means single nano-particle (NP) as small as 40 nm diameter on top of bovine serum albumin immobilization layer [33]. HFIS offers numerous interesting features, such as the mitigation of the salinity-dependent sensitivity limits imposed by the decay of the electrical potential due to ions accumulating at the electrode-electrolyte interface (Debye screening), and the inspection of frequency-dependent electrical properties of analytes for fingerprinting. Moreover, the compatibility with CMOS technology enables a high degree of miniaturization, parallel operation at multiple sensing sites and possibly mass production at low costs. Dimensional scaling of the array along the progress of Moore's law points toward label-free single-particle detection and imaging with better-than-optical nanoscale resolution [33], [34]. Despite a few recent reports of impedance measuring systems with electrode arrays [37], [38], [39], [40], [41], [42], [43], [44], the platform employed in this work remains one of the best in terms of array and electrode size, spatial and capacitance resolution, maximum frequency [33], [45].

This work investigates the potential and challenges of HFIS with CMOS-based NE arrays for detection of nano-pollutants in aqueous solutions. In particular, we examine, by experimental analysis assisted by numerical simulations, the detection of polystyrene (PS) NPs, which is a common water pollutant [4], [7], [15], with sub nanoelectrode pitch dimensions dispersed in phosphate buffer saline (PBS), as well as their size and concentration estimation. The chosen medium has a physiological salt concentration (≈160 mM) matching biological samples, and comparable to seawater, brackish water, and some types of freshwater.

In the following, we denote polymeric spheres with diameter smaller than 1 μm as "nano-plastic" and debris within the same size limits as NPs in general, in agreement with recent published reviews [7], [10], [15], [16], [17], [46]. In addition, although some publications denote "real-time measurements" the ones that operators perform on site of sampling, we prefer to name "continuous flow" those measurements without an operator that could be implemented online at non-zero flow rate, for instance, along a bypass pipe.

This article proceeds as follows. Section II describes the experimental setup, the measurements procedure, and the numerical simulation methods used to assist data interpretation. Section III reports the results of size and concentration estimation; Section IV discusses their significance.

II. MATERIALS AND METHODS

A. Experimental Setup

In this work, we use the HFIS NE array sensor chip (see Fig. 1) extensively described in [33], [34], [35], [36], and [47]. For the sake of a self-contained paper, we summarize in the following its key features. The chip integrates 256×256 individually addressable NEs (radius 90 nm, pitch $p_x \times p_y = 600 \times 720$ nm) fabricated with 90 nm low-power CMOS technology. The calibrated chip provides frequency resolved 256×256 pixels images of the capacitance measured at each electrode in the 1–70 MHz range [33], [36], with potential extension up to 500 MHz [45]. The sensing information is derived as the capacitance change caused by the perturbation of the ac electric field induced by the analyte(s)

$$\Delta C = C_{\text{mean,w/analyte}} - C_{\text{mean,wo/analyte}} \tag{1}$$

where C_{mean} refers to the mean value of 100 samples of the measured capacitance (as described in [33]). Fig. 2 reports an example of capacitance signal with the NP detection event and the resulting ΔC map.

In our nomenclature, the term *mean* refers to the temporal mean, while *average or ave* and *std* refer to the mean and standard deviation over sample space, respectively (e.g., the ensamble of NPs or NEs in the array). The ΔC of each NE is mainly related to the analyte's conductivity and dielectric permittivity, dimensions, and position with respect to the electrodes [33], [48], [49].

The HFIS NE array chip is integrated in an experimental setup (Fig. 1) that includes: 1) the chip's initialization
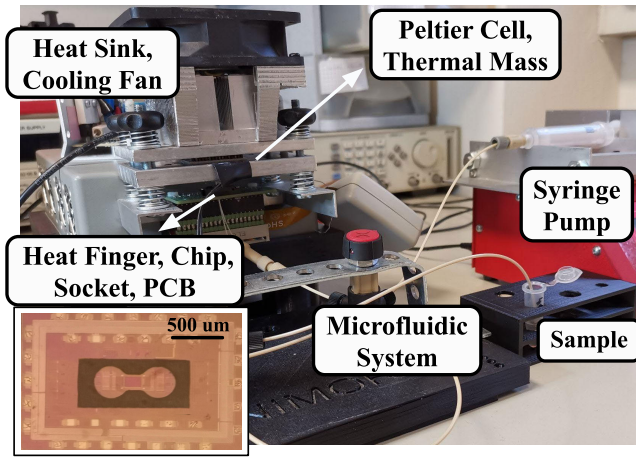
Fig. 1. Picture of the experimental setup. A magnification of the chip with on top the PDMS seal ring around the NE array is also shown.

and interrogation electronics [field programmable gate array (FPGA) board by Intel and custom dual layer printed circuit board (PCB)]; 2) the temperature control system (Peltier cell model ET-127-10-13-RS by adaptive, proportional–integral–derivative (PID) temperature controller model PR-59 by Laird Technologies); 3) the microfluidic chamber confinement around the NE array (socket by ARIES electronics and a novel dogbone shaped polydimethylsiloxane (PDMS) ring, optimized to enhance the probability of analytes passing above the sensing array); and 4) the microfluidic system (polyether-ether-ketone (PEEK) tubes by Upchurch Scientific, step-motor syringe pump model NE-300 by KF-Technology, 10 mL Luer Lock disposable syringe by Cole Parmer, 1.5 mL safe-lock tubes by Eppendorf). More information about each sub-system are given in [33].

B. Numerical Simulation Setup

Numerical simulations of the sensor response to the measured analytes are based on ENBIOS [50], which self-consistently solves the Poisson–Boltzmann equation and the coupled Poisson-Drift-Diffusion equations in steady state and in the time-harmonic, linear small signal regime (AC), respectively, for all ion species in the electrolyte [50]. The capacitance response in the switching regime adopted by the hardware ($\Delta C^{(s)}$) is derived from the AC simulations as described in [33]. The effectiveness of this procedure in accurately reproducing, predicting and supporting interpretation of the sensor acquisitions has been proven in numerous previous studies [33], [34], [35], [48], [49], [50], [51]. Fig. 2 defines the main geometrical and physical parameters used in this work. The simulation grid is created with Netgen [52] and extends over a 5×5 array of NEs with the same radius and pitch as the chip, Section II-A. The NP is implemented as a sphere with radius R and position $(d_x, d_y, d_z + R)$ with respect the center of the central electrode of the 5×5 array [hereafter denoted as pixel (0, 0), which is, by definition, the one which gives the higher ΔC (see Fig. 2)]. The NP permittivity ($\varepsilon_{r,NP}$) and conductivity (σ_{NP}), as well as the dielectric permittivity and the ion concentrations in the electrolyte, are assigned consistently with experiments, as reported in Table II.
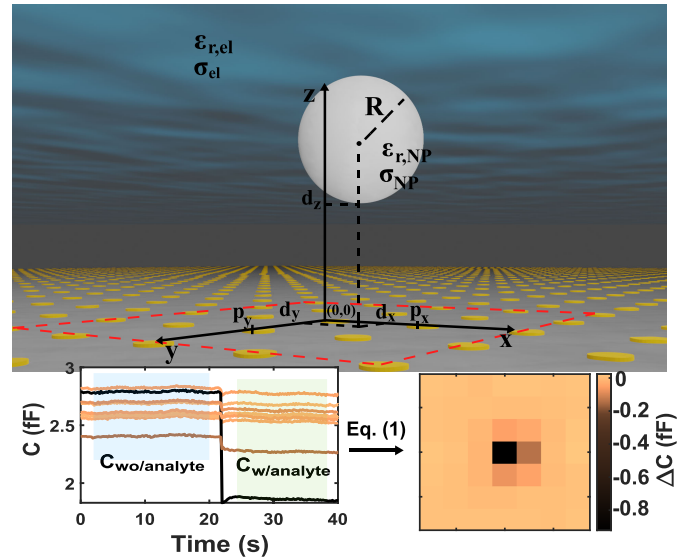

Fig. 2. Sketch of a spherical NP on the NE array immersed in the electrolyte, with the definition of the main geometrical parameters (top). The 5×5 sub-array, centered in pixel (0, 0) is highlighted with a red dashed-line. Capacitance signal from NEs showing the arrival of a 500 nm NP on the sensor surface (bottom left), and resulting 7×7 ΔC map according to (1) (bottom right).

TABLE II
EXPERIMENT/SIMULATION PARAMETERS

[Na]	157 mM	$\varepsilon_{r,NP}$	2.5
[Cl]	140 mM	σ_{NP}	0 S/m
[K]	4.5 mM	$\varepsilon_{r,el}$	80
[HPO_4]	10 mM	Temperature	22 °C
[H_2PO_4]	1.8 mM	Measuring Frequency	50 MHz

C. Experiments and Data Pre-Processing

Polystyrene NPs (PS-NPs) with nominal radii (R_{nom}) of 50 ± 2.5 nm (Merck KGaA- Sigma-Aldrich, Germany), 275 ± 8 nm, and 500 ± 5 nm (Polysciences Inc, USA), were used in this work. The PS-NPs are suspended in 15 mL aqueous solutions of 10%, 2.74%, and 2.66% (w/v) respectively. As stated before, the NPs were analyzed in PBS $1\times$ (NaCl 137 mM + KCl 2.7 mM+ Na$_2$HPO$_4$ 10 mM + KH$_2$PO$_4$ 1.8 mM, Merck KGaA- Sigma-Aldrich, Germany). The procedure to create the NPs-PBS sample is the following.

1) The PBS was filtered with 0.2 μm pores syringe filter (Puradisc 25 mm, in PES, by Whatman) to remove possible impurities.
2) Each PS-NPs solution was added to a proper volume of filtered PBS to obtain lower and comparable nominal concentrations: $9.5 \cdot 10^9$, $7.86 \cdot 10^9$, and $1.27 \cdot 10^9$ #NP/mL for samples with radius 50, 275, and 500 nm, respectively.
3) The diluted NPs-PBS sample was filtered with 3 μm pores syringe filter membrane (Fluoropore, 47 mm, PTFE, by Millipore) and sonicated (Cole Parmer CPX-750 Ultrasonic Homogenizer) before and after the filtering. The NPs size was also measured with dynamic light scattering (DLS), a common NP size estimation method [53]. We obtained measured DLS radii 53.8 ± 6,

278.3 ± 28, and 500.4 ± 30 nm, essentially confirming the reported nominal values. Therefore, the nominal values will be taken as reference below.

Once the sample was prepared, the following measurement procedure was carried out.

1) The chip's platform and the temperature control system were turned on, the chosen measurement conditions were set (see Table II) and the system was allowed to reach the thermal steady state.
2) The microfluidic system was flushed with ≈3 mL isopropyl alcohol (IPA, purchased by Sigma-Aldrich), filtered with 0.2 μm pores syringe filter, with a flow rate of 100 μL/min. This procedure cleans the tubes and the NE array, eliminates air bubbles, and allows us to eliminate upfront possible fluid leakages.
3) The system was briefly flushed with ≈1 mL of PBS, to minimize undesired mixing of the NPs sample with IPA.
4) The NPs-PBS sample is introduced into the microfluidics.
5) Once the data were collected, the system was flushed with ≈3 mL of deionized H_2O (Sigma-Aldrich, Germany), filtered with 0.2 μm pores syringe filter, and ≈3 mL of IPA with a flow rate of 200 μL/min for cleaning.

The ambient temperature was ≈22 °C, equal to the temperature controller setpoint; therefore the fluid temperature does not affect the measurement.

Three experiments were performed for radius and concentration estimation, one for each NP. Overall, more than 100 objects were analyzed for each radius. Additionally, five tests were run with 500 nm radius NPs to estimate concentration at different dilutions. In particular, starting from nominal concentration $n_P = 1.27 \cdot 10^9$ #NP/mL, dilutions of 1:2, 1:5, 1:10, and 1:20 were considered. Experiments were repeated with the latter samples according to the above procedure. In order to investigate static and continuous flow conditions, the flow rate ϕ_n was initially set to zero, and then to 10, 100, 10, and again 10 μL/min, each for a time interval $T_n \approx 75$ s for total examined volume $V_{\text{sample}} = \sum_n \phi_n \cdot T_n = 158$ μL, equal for each concentration value.

Finally, the data were elaborated according to [33] and a 5×5 $\Delta C(i, j)$ matrix centered on the electrode (0,0) with maximum response $\Delta C(0, 0)$ was calculated with (1) after the object detection procedure. Given the large amount of raw data generated by the experiments (≈246 MB/min), and the upfront lack of a robust object detection algorithm, the NPs detection was only partially automated during the first experiments. In particular, we applied the MATLAB function *findchangepts* on the capacitance signal of each NE to extract the instants when the measured capacitance significantly changes its mean value (detection event). Then, we calculated $C_{\text{mean,w/analyte}}$ and $C_{\text{mean,wo/analyte}}$ from values respectively following and preceding the particle arrival event. Last, the NPs in the first experiments (Section III-A) were identified manually to form a dataset of ≈300 objects (≈100 for each NP size). Once the radius estimation model was derived, for the concentration estimation, a simple automated object detection algorithm for monodisperse solutions (described in Section II-D2) was used to identify the right objects in the image, count them and then estimate the NPs concentration, $n_{P,\text{est}}$. In this way the NPs concentration estimation is not operator-dependent, and the radius estimation model was also validated on new, automatically detected sets of particles with respect to the previously manually selected 300 NPs.

D. Methods for Size and Concentration Estimation

1) Sub-Pitch Radius Estimation: Size estimation for NPs with dimensions smaller than the pitch of the imaging array (50–500 nm NP radius and pitch $p_x = 600$ nm, $p_y = 720$ nm), poses new challenges with respect to existing water-pollutants monitoring systems [15] and to previous works on this same platform but with larger microparticles [33], [35], [48]. Three aspects can be interdependently taken into consideration: 1) at high enough frequency, the AC electric field propagated in the electrolyte by one electrode spreads laterally beyond one pitch distance [33]; 2) the ΔC magnitude is proportional to the particle volume (thus, to the cube of its radius) [49]; and 3) possible displacement of the NP in the 2-D plane can result in a significant response of adjacent electrodes. Since sub-pitch sizes are considered, only a 3×3 matrix is examined, to avoid adding data from electrodes with very small and noisy response to the NP.

Based on these considerations, we first estimated the particle offset in x- and y-directions (d_x and d_y, see Fig. 2) with respect to the electrode featuring the highest response as follows:

$$d_{x,\text{est}} = \frac{\sum_{i,j} |\Delta C(i, j)| \cdot i \cdot p_x}{\sum_{i,j} |\Delta C(i, j)|} \quad (2)$$

$$d_{y,\text{est}} = \frac{\sum_{i,j} |\Delta C(i, j)| \cdot j \cdot p_y}{\sum_{i,j} |\Delta C(i, j)|} \quad (3)$$

where $(i, j) \in [(-1, +1), (-1, +1)]$, with $p_x = 600$ nm and $p_y = 720$ nm. Then we calculated

$$d(i, j)^2 = (d_{x,\text{est}} + i \cdot p_x)^2 + (d_{y,\text{est}} + j \cdot p_y)^2 \quad (4)$$

which represents the 3×3 matrix of distances of each first neighbor pixel from the pixel with largest response (i.e., the coordinates origin) shifted according to the NP position ($d_{x,\text{est}}, d_{y,\text{est}}$) estimated using (2) and (3). Exploiting symmetry reasons, we constructed a four elements vector $\gamma(e)$ by averaging $[\Delta C(i, j)d^2(i, j)]/C_0$ over symmetric pixel locations: $e = 1$ for $(i, j) = (0, 0)$, $e = 2$ for $(i, j) = (\pm 1, 0)$, $e = 3$ for $(i, j) = (0, \pm 1)$, and $e = 4$ for $(i, j) = (\pm 1, \pm 1)$. Here C_0 is the ensemble average capacitance measured by the chip NEs in dry air at 50 MHz and $T = 22$ °C. Eventually, we expressed the estimated particle radius as follows:

$$R_{\text{est}} = \sqrt{\sum_e p(e) \cdot \gamma(e)} \quad (5)$$

where $p(e)$ is a vector of calibration coefficients, actually taken all equal in this work. This reduces the model parameters to only one scalar value p. From a single experiment with NPs of nominal radius R_{nom} detecting N_{data} objects, the mean

value $\overline{R}$, the uncertainty u_R, and the prediction error ϵ_R were calculated according to

$$\overline{R} = \frac{1}{N_{\text{data}}} \sum_i^{N_{\text{data}}} R_{\text{est},i} \tag{6}$$

$$u_R = \sqrt{\frac{1}{N_{\text{data}}(N_{\text{data}} - 1)} \cdot \sum_i^{N_{\text{data}}} (R_{\text{est},i} - \overline{R})^2} \tag{7}$$

$$\epsilon_R\% = \frac{\overline{R} - R_{\text{nom}}}{R_{\text{nom}}} \cdot 100. \tag{8}$$

2) Noise-Based Sensing Volume Definition for Concentration Estimation: The accurate determination of NPs concentration (n_P) requires to quantify the volume inspected by the measurement system, hereafter called sensing volume, V_{sens}. This is a challenging task for sensors based on impedance measurement, due to the rapid decay of the electric field magnitude induced by Debye screening, and the hypersensitivity of low frequency measurements to surface phenomena. In fact, Debye screening is largely dependent on measurement frequency and ionic concentration [34]. Since, at first order, the NE capacitance response ΔC is proportional to the squared *unperturbed* AC electric field at the particle center location (i.e., the one in the absence of a particle, denoted E^2) [49], we can define the sensing volume as the region above the array surface where the squared *unperturbed* AC electric field is larger than the threshold value (E_{thr}^2) that corresponds to $\Delta C_{\text{thr}} = 3 \cdot \sigma_{\text{noise,ave}}$, where $\sigma_{\text{noise,ave}}$ is the ensemble experimental standard deviation of the electrode capacitance measured in the absence of analytes. The dominant noise generation mechanism is electronic, as discussed in [33].

In practice, the following procedure was used to calculate V_{sens} for each NP radius. First, a statistical analysis of the capacitance noise from experiments without NPs was performed. In particular, we verified that: 1) in the chosen conditions (see Table II), the ΔC noise of each electrode was Gaussian with zero mean and 2) the measured $\sigma_{\text{noise}}(i, j)$, i.e., the empirical standard deviation of the ΔC, was homogeneously distributed over the entire array ($(i, j) \in [(1, 256), (1, 256)]$), i.e., $\sigma_{\text{noise,std}} \ll \sigma_{\text{noise,ave}}$, where $\sigma_{\text{noise,ave}}$ and $\sigma_{\text{noise,std}}$ are the empirical average and standard deviation of σ_{noise} of the ensemble of all 256 × 256 electrodes. If these were verified, we assumed that all electrodes behave the same and the maximum sensing distance was essentially constant above all electrodes, regardless of i and j. Second, exploiting the available accurate simulation setup, we determined the threshold distance $d_{z,\text{thr}}$, such that the simulated $\Delta C^{(s)}(dz > d_{z,\text{thr}}) < \Delta C_{\text{thr}}$, and the corresponding $E_{\text{thr}}^2 = E^2(0, 0, d_{z,\text{thr}} + R_{\text{nom}})$. The electrolyte region where $z_{\text{sens}}(x, y) = d_{z,\text{thr}} + R_{\text{nom}}$ such that for $z < z_{\text{sens}}(x, y)$: $E^2(x, y, z) > E_{\text{thr}}^2$ defines a surface in the 3-D space over a single electrode. Thus, exploiting the generalization verified in the first step, V_{sens} is

$$V_{\text{sens}} = \sum_{i=1}^{256} \sum_{j=1}^{256} \iint_\Omega z_{\text{sens}} \, dx \, dy \tag{9}$$

where Ω is the portion of the array corresponding to a single electrode

$$\Omega = \{(x, y) : \ x \in [-300, \ 300] \text{ nm}, \ y \in [-360, \ 360] \text{ nm}\}.$$

Note that, for the calculation of V_{sens} the knowledge of the salinity of the sample is necessary, for instance by advanced techniques as those reported in [54] and [55].

Once V_{sens} was calculated, the NP concentration (n_P) was estimated according to

$$n_{P,\text{est}} = \lambda \cdot \zeta \cdot \frac{N_P}{\left(V_{\text{chamber}} + \sum_n \phi_n \cdot T_n\right)} \tag{10}$$

where N_P is the cumulative number of NPs detected in a given experiment, V_{chamber} is the volume of the measuring chamber ($A_{\text{array}} \cdot z_{\text{max}} \simeq 7.1$ nL). ϕ_n is the flow rate set for time T_n (as described in Section II-C, for experiments evaluating continuous measurements $\sum_n \phi_n \cdot T_n = 158$ μL). $\zeta = V_{\text{chamber}}/V_{\text{sens}}$ is the coefficient that takes into account the reduction of the volume inspected by the NE array with respect the total V_{chamber}. Finally, the correction factor λ (derived experimentally) reflects the observation that in continuous flow measurement (i.e., non-zero flow rate) N_P did not scale proportionally to the flowing sample volume. Thus, λ is taken equal to 1 in case of static measurements, whilst $\lambda \neq 1$ in continuous flux conditions. N_P was computed with the following procedure: the MATLAB function *findchangepts* was used to detect significant variations of mean capacitance for each electrode, as described before. Afterward, the radius estimation model described in Section II-D1 was used to filter non-NP events (noise, local drifts, bubble, impurities, etc...) defined as $R_{\text{est}} < 0.5 \cdot R_{\text{nom}}$ and $R_{\text{est}} > 1.2$ μm (consistently with the choice to consider a 3×3 array with approximate size 1.2×1.44 μm), R_{nom} being the nominal radius of the monodisperse NPs. Finally, the concentration estimation error was calculated as follows:

$$\epsilon_{n_P}\% = \frac{n_{P,\text{est}} - n_{P,\text{nom}}}{n_{P,\text{nom}}} \cdot 100. \tag{11}$$

III. RESULTS

A. Sub-Pitch Size Estimation

As described in Section II-D1, the unit-less coefficient of the radius estimation model was calibrated on measurements (300 objects) obtaining $p = -434.4$, while the average capacitance in air at 50 MHz and $T = 22$ °C is $C_0 \simeq 0.40$ fF. Fig. 3 shows the predicted nominal radius, whereas Table III reports model prediction results ($\overline{R} \pm u_R$) and errors ($\epsilon_R\%$) according to (6)–(8). Further validation of the radius estimation model is reported in Section III-B, where the model was used to automate the NPs detection for n_P estimation.

B. Concentration Estimation

Fig. 4 (left) shows the probability density function (PDF) of the σ_{noise} measured for each electrode in four experiments without analytes, at zero flow rate and conditions reported in Table II. Each σ_{noise} was calculated from 200 capacitance measurements per electrode, and the mean value of the noise is zero. The figure also shows $\sigma_{\text{noise,ave}}$ (red dashed line).
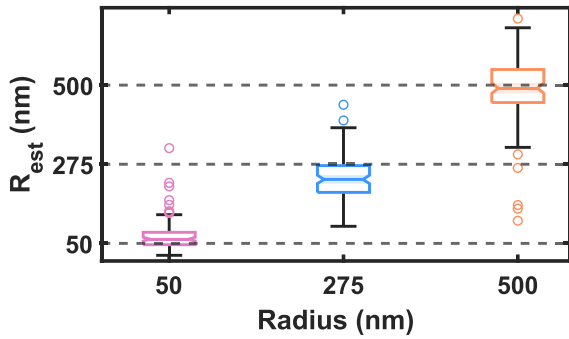
Fig. 3. Results of radius estimation model according to Section II-D1 for all NPs (R_{est} versus R_{nom}). Aggregate results are reported in Table III.

TABLE III
NOMINAL AND PREDICTED NP RADIUS AND ESTIMATION ERROR

Nominal Radius (nm)	Predicted Radius ($\bar{R} \pm u_R$ nm)	Prediction Error (ϵ_R %)
50 ± 2.5	72.66 ± 4.4	45.32
275 ± 8	235.29 ± 5.7	-14.44
500 ± 5	486.48 ± 9.5	-2.70
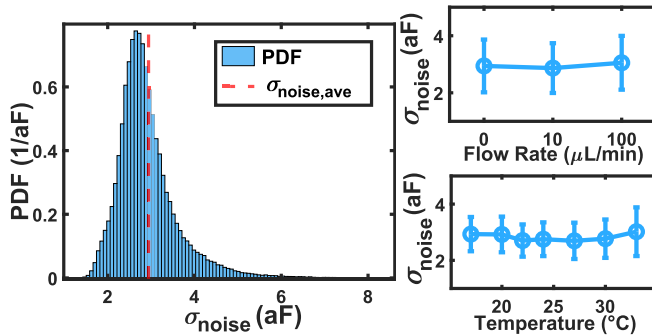
Fig. 4. Distribution of σ_{noise} for all electrodes in four different experiments ($\phi = 0 \ \mu L/min$, 22 °C, 50 MHz), the resulting ensemble $\sigma_{noise,ave}$ is also shown (left). $\sigma_{noise,ave} \pm \sigma_{noise,std}$ for different flow rate and temperature values (right).

Fig. 5. Simulated capacitance change due to the NP $-\Delta C^{(s)}$ with $d_x = 0$, $d_y = 0$, as a function of d_z (top). Intersection with $3 \cdot \sigma_{nosie,ave}$ is $d_{z,thr}$. V_{sens} calculated according to (9) as a function of the radii considered (bottom).

Fig. 6. Radius estimation error for each case (top). Concentration estimation error ϵ_{np} (mean value $\pm u_\epsilon$) as a function of the radius calculated as (7) in stationary conditions ($\phi = 0$) (bottom).

The resulting value of $\sigma_{noise,ave}$ is 2.9 aF, with a standard deviation $\sigma_{noise,std}$ of 0.7 aF. Fig. 4 (right) shows $\sigma_{noise,ave} \pm \sigma_{noise,std}$ for varying flow rates at $T = 22$ °C (top) and for zero flow rate and varying temperatures (bottom), showing stable values regardless of the considered environmental conditions.

Following the method described in Section II-D2, $d_{z,thr}$ and E_{thr}^2 were calculated from numerical simulations to determine V_{sens}. Fig. 5 (top) shows the simulated $\Delta C^{(s)}$ as a function of d_z for particles centered on the electrode, as discussed in Section II-D2. The intersections of the curves with the $3 \cdot \sigma_{noise,ave}$ threshold yields $d_{z,thr}$. Fig. 5 (bottom) shows the corresponding V_{sens} in log-scale for different radii.

Fig. 6 (bottom) shows the concentration error under stationary conditions ($\phi = 0$, $\lambda = 1$) according to (11) versus the nominal radius. The estimated n_P is the average over four V_{sens} calculations at $\phi = 0 \ \mu L/min$ and four different instants. Fig. 6 (top) shows the corresponding radius estimation error in boxcharts; as discussed in Section II-D2, the radius estimation was part of the automated procedure for NPs detection.
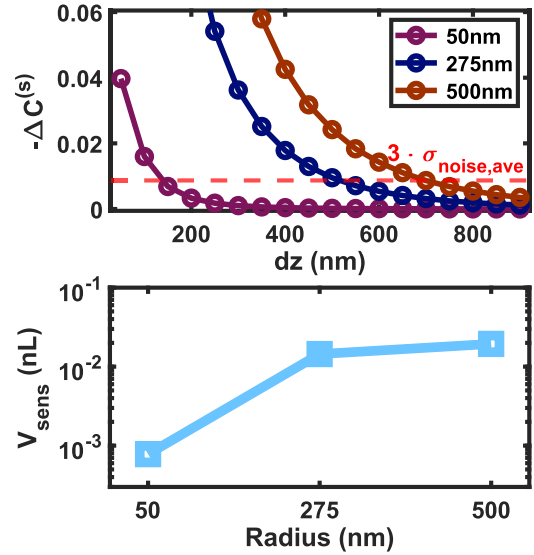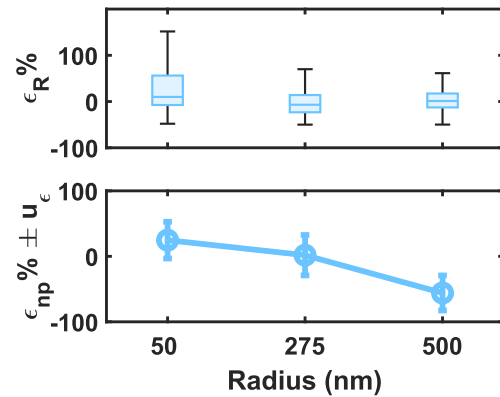
In agreement with results reported in Section III-A, we observe that the model overestimates the expected value for 50 nm NPs, and also has larger spread.

Fig. 7 shows the results of experiments where dilution was varied, and where continuous measurements (with flux) were investigated. The unit-less correction factor λ is 1 at zero flow and 1740 otherwise. The top graph shows the estimated concentration in this case versus the nominal concentration. The middle graph reports the estimated radius for each concentration value, showing predictions independent of concentration, as it should be. The bottom graph shows the concentration estimation error under both steady ($\phi = 0$) and continuous flow ($\phi \neq 0$) conditions. While V_{sens} calculation enables concentration estimation, further optimization of the measurement chamber may be necessary to improve the accuracy and efficiency of the measurement. In fact, since the NPs outside V_{sens} are not detectable by the NE array, the height of the measuring chamber can be optimized guiding the sample
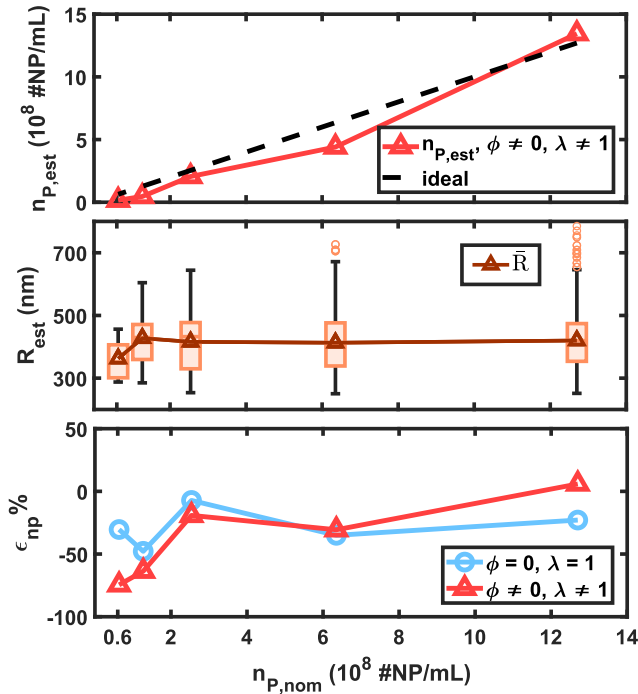
Fig. 7. Concentration estimated according to (10) versus nominal concentration in the case of continuous measurements (top). Radius estimated in each cases, the mean prediction ($\bar{R}$) is also reported (middle). Concentration estimation wrong symbol (○) and continuous (▲) for different concentration values (bottom).

flow in this region, or the measurement frequency increased to further reduce Debye screening.

IV. DISCUSSION AND CONCLUSION

As anticipated in the introduction, current water pollutant monitoring systems suffer several limitations, particularly so in detecting particles in the nanoscale. This study investigated the potential of a new monitoring paradigm based on high-frequency impedance measurement with CMOS NE arrays for continuous monitoring of nanoparticles in water. An analytical model for size estimation of NPs with (sub-pitch) radii smaller than the theoretical resolution of the array (pitch 600 × 720 nm) has been developed. Compared to nominal values, the model slightly underestimates larger NP dimensions (275, 500 nm), while overestimating those with smaller radii (50 nm). Nevertheless, the worst case mean error is always lower than 45%. The spread of the estimated radii (Table III, Fig. 3) is only slightly larger than the nominal one, and essentially in line with DLS sizing experiments, which confirmed very low deviations (<7%) from the nominal NP radii. Possibly, the slightly larger variability in the measured capacitance may reflect that of the unknown vertical position of the particle.

We also addressed the challenging goal of estimating the concentration of PS-NPs in stationary and continuous flow conditions, as a model system for more general nano-plastic monitoring in water. Our approach defines the sensing volume and accounts for it considering the noise associated with the capacitance measurement of the nanoelectrodes. Promising results are obtained for all NP concentrations (Figs. 6 and 7)

and for different radii. They demonstrate a worst case estimation error of a factor 1.7.

Notice that all experiments were run in high ionic strength solutions (PBS ~160 mM) compared, for instance, to common tap water. Although Debye screening limitations are mitigated at the chosen 50 MHz operating frequency, the sensing distance remains much smaller than the microfluidic chamber height; therefore, our evaluations may be overpessimistic with respect to tap water conditions of large interest. We also point out that the simple analytical models proposed to extract R_{est} and n_P rely on only two calibration parameters, easily estimated from two dedicated experiments which is a valuable feature in view of low-power Internet of Things (IoT) applications.

Several aspects deserve more extensive future investigations. First, the estimation of the nano-plastics surface charge density, which recent papers suggest to play an important role in NPs cytotoxicity [10], [56], is definitely in the potential of the HFIS CMOS NE array, thanks to its spectrally resolved operating mode and large bandwidth. Second, since capacitance spectroscopy is sensitive to the dielectric permittivity and conductivity of the analyte, a potential for NP material classification of pollutants exists. Common plastic pollutants (e.g., polystyrene, PVC, and PET) have similar ε_r (in the 2–4 range); discrimination among their responses appears challenging given the electronic noise floor of current chip implementations and the variability of the response induced by the unknown position above the array surface. On the contrary, discrimination between dielectric and metallic NPs (and likely materials in between) is possible via inspection of the measured ΔC, whose sign depends on the conductive versus dielectric nature of the analyte, and is likely improved by fingerprinting of the capacitance spectra as shown in [35] and [34]. The explored concentrations interval is on the high side for common micro and nano pollutants' concentration in water. Furthermore, aggregates have been avoided via sonication, but should be part of more extensive studies beyond the scope of this work. Notwithstanding all the above considerations, to the best of our knowledge, this is the only CMOS electronic sensing technology reporting single nanoparticle detection *and* size/concentration estimation in continuous flow with NP radii down to 50 nm to date.

REFERENCES

[1] *Guidelines for Drinking-Water Quality: Fourth Edition Incorporating the First and Second Addenda*, World Health Organization, Geneva, Switzerland, 2022.

[2] K. H. Vardhan, P. S. Kumar, and R. C. Panda, "A review on heavy metal pollution, toxicity and remedial measures: Current trends and future perspectives," *J. Mol. Liquids*, vol. 290, Sep. 2019, Art. no. 111197.

[3] P. Roy, A. K. Mohanty, and M. Misra, "Microplastics in ecosystems: Their implications and mitigation pathways," *Environ. Sci., Adv.*, vol. 1, no. 1, pp. 9–29, 2022.

[4] A. Yusuf et al., "Updated review on microplastics in water, their occurrence, detection, measurement, environmental pollution, and the need for regulatory standards," *Environ. Pollut.*, vol. 292, Jan. 2022, Art. no. 118421.

[5] E. Danopoulos, M. Twiddy, and J. M. Rotchell, "Microplastic contamination of drinking water: A systematic review," *PLoS ONE*, vol. 15, no. 7, Jul. 2020, Art. no. e0236838.

[6] H. A. Leslie, M. J. M. van Velzen, S. H. Brandsma, A. D. Vethaak, J. J. Garcia-Vallejo, and M. H. Lamoree, "Discovery and quantification of plastic particle pollution in human blood," *Environ. Int.*, vol. 163, May 2022, Art. no. 107199.

[7] S. Sangkham et al., "A review on microplastics and nanoplastics in the environment: Their occurrence, exposure routes, toxic studies, and potential effects on human health," *Mar. Pollut. Bull.*, vol. 181, Aug. 2022, Art. no. 113832.

[8] N. Jan, N. Majeed, M. Ahmad, W. A. Lone, and R. John, "Nanopollution: Why it should worry us," *Chemosphere*, vol. 302, Sep. 2022, Art. no. 134746.

[9] L. K. Bhardwaj, P. Rath, and M. Choudhury, "A comprehensive review on the classification, uses, sources of nanoparticles (NPs) and their toxicity on health," *Aerosol Sci. Eng.*, vol. 7, no. 1, pp. 69–86, Mar. 2023.

[10] N. P. Ivleva, "Chemical analysis of microplastics and nanoplastics: Challenges, advanced methods, and perspectives," *Chem. Rev.*, vol. 121, no. 19, pp. 11886–11936, Oct. 2021.

[11] M. Enfrin, J. Lee, Y. Gibert, F. Basheer, L. Kong, and L. F. Dumée, "Release of hazardous nanoplastic contaminants due to microplastics fragmentation under shear stress forces," *J. Hazardous Mater.*, vol. 384, Feb. 2020, Art. no. 121393.

[12] F. J. Millero, *Chemical Oceanography*, 4th ed. CRC Press, 2013, doi: 10.1201/b14753.

[13] World Health Organization. (2019). *WHO Calls for More Research Into Microplastics and a Crackdown on Plastic Pollution*. [Online]. Available: https://www.who.int/news/

[14] J. C. Prata, J. P. da Costa, A. C. Duarte, and T. Rocha-Santos, "Methods for sampling and detection of microplastics in water and sediment: A critical review," *TrAC Trends Anal. Chem.*, vol. 110, pp. 150–159, Jan. 2019.

[15] J. Lee and K.-J. Chae, "A systematic protocol of microplastics analysis from their identification to quantification in water environment: A comprehensive review," *J. Hazardous Mater.*, vol. 403, Feb. 2021, Art. no. 124049.

[16] N. B. Hartmann et al., "Are we speaking the same language? Recommendations for a definition and categorization framework for plastic debris," *Environ. Sci. Technol.*, vol. 53, no. 3, pp. 1039–1047, Feb. 2019.

[17] J. R. Bermúdez and P. W. Swarzenski, "A microplastic size classification scheme aligned with universal plankton survey methods," *MethodsX*, vol. 8, Jan. 2021, Art. no. 101516.

[18] V. Meiler, J. Pfeiffer, L. Bifano, C. Kandlbinder-Paret, and G. Fischerauer, "Approaches to detect microplastics in water using electrical impedance measurements and support vector machines," *IEEE Sensors J.*, vol. 23, no. 5, pp. 4863–4872, Mar. 2023.

[19] S. Oh et al., "On-site/in situ continuous detecting ppb-level metal ions in drinking water using block loop-gap resonators and machine learning," *IEEE Trans. Instrum. Meas.*, vol. 70, pp. 1–9, 2021.

[20] O. Malyuskin, "Microplastic detection in soil and water using resonance microwave spectroscopy: A feasibility study," *IEEE Sensors J.*, vol. 20, no. 24, pp. 14817–14826, Dec. 2020.

[21] J. Mahato, C. R. Raj, and K. Biswas, "Low-noise potentiostat circuit for electrochemical detection of heavy metals or metalloids," *IEEE Trans. Instrum. Meas.*, vol. 71, pp. 1–9, 2022.

[22] P. Wang et al., "A real-time water quality measurement instrument for simultaneously detecting turbidity and particle size by using single-photon counting technique," *IEEE Trans. Instrum. Meas.*, vol. 71, pp. 1–6, 2022.

[23] S. Battula, M. Kumar, S. K. Panda, K. Pavan, and U. Rao, "In-situ microplastic detection sensor based on cascaded microring resonators," in *Proc. OCEANS, San Diego Porto*, Sep. 2021, pp. 1–5.

[24] D. G. Kotsifaki, C. Ripken, and S. N. Chormaic, "Detection and analysis of microplastics in the subtropical ocean of Okinawa using micro-Raman optical tweezers," in *Proc. Int. Workshop Metrol. Sea; Learn. Measure Sea Health Parameters (MetroSea)*, Oct. 2021, pp. 158–162.

[25] A. H. Iri et al., "Optical detection of microplastics in water," *Environ. Sci. Pollut. Res.*, vol. 28, no. 45, pp. 63860–63866, Dec. 2021.

[26] M. Shafiei, Z. Abbasi, and C. L. Ren, "Passive disposable microwave sensor for online microplastic contamination monitoring," in *IEEE MTT-S Int. Microw. Symp. Dig.*, Jun. 2022, pp. 263–266.

[27] J. H. Kim, K. H. Lee, C. U. Cha, and Y. T. Hong, "PDMS-based RF resonant sensor for measuring the concentration of micro-plastics," in *Proc. IEEE Int. Conf. Ind. Eng. Eng. Manage. (IEEM)*, Dec. 2021, pp. 293–296.

[28] X. Wang, Y. Wang, H. Leung, S. C. Mukhopadhyay, M. Tian, and J. Zhou, "Mechanism and experiment of planar electrode sensors in water pollutant measurement," *IEEE Trans. Instrum. Meas.*, vol. 64, no. 2, pp. 516–523, Feb. 2015.

[29] J. Lorenzo-Navarro et al., "SMACC: A system for microplastics automatic counting and classification," *IEEE Access*, vol. 8, pp. 25249–25261, 2020.

[30] C. Massarelli, C. Campanale, and V. F. Uricchio, "A handy open-source application based on computer vision and machine learning algorithms to count and classify microplastics," *Water*, vol. 13, no. 15, p. 2104, Jul. 2021.

[31] G. Miele et al., "Electrical impedance spectroscopy for real-time monitoring of the life cycle of graphene nanoplatelets filters for some organic industrial pollutants," *IEEE Trans. Instrum. Meas.*, vol. 70, pp. 1–12, 2021.

[32] L. Ilerioluwa et al., "A multi-parameter microfluidic particle sensor based on permalloy for high sensitivity," *IEEE Trans. Instrum. Meas.*, vol. 71, pp. 1–10, 2022.

[33] F. Widdershoven et al., "A CMOS pixelated nanocapacitor biosensor platform for high-frequency impedance spectroscopy and imaging," *IEEE Trans. Biomed. Circuits Syst.*, vol. 12, no. 6, pp. 1369–1382, Dec. 2018.

[34] C. Laborde et al., "Real-time imaging of microparticles and living cells with CMOS nanocapacitor arrays," *Nature Nanotechnol.*, vol. 10, no. 9, pp. 791–795, Sep. 2015.

[35] A. Cossettini, C. Laborde, D. Brandalise, F. Widdershoven, S. G. Lemay, and L. Selmi, "Space and frequency dependence of nanocapacitor array sensors response to microparticles in electrolyte," *IEEE Sensors J.*, vol. 21, no. 4, pp. 4696–4704, Feb. 2021.

[36] F. Widdershoven et al., "CMOS biosensor platform," in *IEDM Tech. Dig.*, Dec. 2010, pp. 36.1.1–36.1.4.

[37] J. Abbott et al., "Multi-parametric functional imaging of cell cultures and tissues with a CMOS microelectrode array," *Lab Chip*, vol. 22, no. 7, pp. 1286–1296, 2022.

[38] K. Hu, C. E. Arcadia, and J. K. Rosenstein, "A large-scale multimodal CMOS biosensor array with 131,072 pixels and code-division multiplexed readout," *IEEE Solid-State Circuits Lett.*, vol. 4, pp. 48–51, 2021.

[39] D. Jung et al., "A CMOS 21 952-pixel multi-modal cell-based biosensor with four-point impedance sensing for holistic cellular characterization," *IEEE J. Solid-State Circuits*, vol. 56, no. 8, pp. 2438–2451, Aug. 2021.

[40] H. Chen, X. Yang, P. Wang, J. Geng, G. Ma, and X. Wang, "A large-area flexible tactile sensor for multi-touch and force detection using electrical impedance tomography," *IEEE Sensors J.*, vol. 22, no. 7, pp. 7119–7129, Apr. 2022.

[41] S. Hu, G. Gao, Z. Hong, C. Liu, K. Liu, and J. Yao, "An electrode array sensor for tongue cancer detection with bioelectrical impedance spectroscopic tomography," *IEEE Sensors J.*, vol. 22, no. 15, pp. 15146–15153, Aug. 2022.

[42] P.-H. Lai, L.-S. Tseng, C.-M. Yang, and M. S.-C. Lu, "Design and characterization of a 16×16 CMOS capacitive DNA sensor array," *IEEE Sensors J.*, vol. 23, no. 8, pp. 8120–8127, Apr. 2023.

[43] S. R. Kumashi et al., "A CMOS multi-modal electrochemical and impedance cellular sensing array for massively paralleled exoelectrogen screening," *IEEE Trans. Biomed. Circuits Syst.*, vol. 15, no. 2, pp. 221–234, Apr. 2021.

[44] J. Liu et al., "Taste analog perception system based on impedance spectrum sensor array and human-like fuzzy evaluation cloud model," *IEEE Sensors J.*, vol. 22, no. 20, pp. 19513–19523, Oct. 2022.

[45] A. Cossettini et al., "Ultra-high frequency (500 MHz) capacitance spectroscopy for nanobiosensing," in *Proc. IEEE Sensors*, Oct. 2020, pp. 1–4.

[46] F. Caputo et al., "Measuring particle size distribution and mass concentration of nanoplastics and microplastics: Addressing some analytical challenges in the sub-micron size range," *J. Colloid Interface Sci.*, vol. 588, pp. 401–417, Apr. 2021.

[47] B. Stadlbauer et al., "Bayesian estimation of physical and geometrical parameters for nanocapacitor array biosensors," *J. Comput. Phys.*, vol. 397, Nov. 2019, Art. no. 108874.

[48] A. Cossettini, B. Stadlbauer, J. A. Morales E., L. Taghizadeh, L. Selmi, and C. Heitzinger, "Determination of Micro- and nano-particle properties by multi-frequency Bayesian methods and applications to nanoelectrode array sensors," in *Proc. IEEE Sensors*, Oct. 2019, pp. 1–4.

[49] F. Pittino, P. Scarbolo, F. Widdershoven, and L. Selmi, "Derivation and numerical verification of a compact analytical model for the AC admittance response of nanoelectrodes, suitable for the analysis and optimization of impedance biosensors," *IEEE Trans. Nanotechnol.*, vol. 14, no. 4, pp. 709–716, Jul. 2015.

[50] F. Pittino and L. Selmi, "Use and comparative assessment of the CVFEM method for Poisson–Boltzmann and Poisson–Nernst–Planck three dimensional simulations of impedimetric nano-biosensors operated in the DC and AC small signal regimes," *Comput. Methods Appl. Mech. Eng.*, vol. 278, pp. 902–923, Aug. 2014.

[51] A. Cossettini and L. Selmi, "On the response of nanoelectrode impedance spectroscopy measures to plant, animal, and human viruses," *IEEE Trans. Nanobiosci.*, vol. 17, no. 2, pp. 102–109, Apr. 2018.

[52] J. Schöberl, "An advancing front 2D/3D-mesh generator based on abstract rules," *Comput. Visualizat. Sci.*, vol. 1, no. 1, pp. 41–52, Jul. 1997.

[53] Z. Jia, J. Li, L. Gao, D. Yang, and A. Kanaev, "Dynamic light scattering: A powerful tool for in situ nanoparticle sizing," *Colloids Interface*, vol. 7, no. 1, p. 15, Feb. 2023.

[54] I. R. Jang et al., "High precision liquid salinity sensing using a CNT coated quartz crystal microbalance," *IEEE Sensors J.*, vol. 22, no. 8, pp. 7684–7691, Apr. 2022.

[55] L. Wang et al., "High-resolution optical fiber salinity sensor with self-referenced parallel Fabry–Pérot fiber microcavity," *IEEE Sensors J.*, vol. 23, no. 1, pp. 337–343, Nov. 2022.

[56] A. Roshanzadeh et al., "Surface charge-dependent cytotoxicity of plastic nanoparticles in alveolar cells under cyclic stretches," *Nano Lett.*, vol. 20, no. 10, pp. 7168–7176, Oct. 2020.

Luigi Rovati (Member, IEEE) is currently a Full Professor of Electronic Instrumentation and Measurement Science with the Department of Engineering "Enzo Ferrari," University of Modena and Reggio Emilia, Modena, Italy. He is also the Scientific Director of the MS2 Laboratory of the Science and Technology Park for Medicine (TPM) "Mario Veronesi," Mirandola, Italy. He has authored more than 200 articles testifies the level of the developed activity. He is also involved in various research projects between university and industrial partners. His research activities have been toward the study and the development of high-performance and innovative instrumentation.

Daniele Goldoni (Graduate Student Member, IEEE) received the B.Sc. degree in biomedical engineering from the University of Bologna, Bologna, Italy, in 2019, and the M.Sc. degree in electronics engineering from the University of Modena and Reggio Emilia, Modena, Italy, in 2021, where he is currently pursuing the Ph.D. degree in advanced integrated electronic biosensors for nanoscale entity detection.

His research activities on electronic and opto-electronic measurement systems for biomedical and environmental application.

Luca Selmi (Fellow, IEEE) received the Ph.D. degree in electronic engineering from the University of Bologna, Bologna, Italy, in 1992.

Since 2000, he has been a Professor of Electronics with the University of Udine, Udine, Italy, and then recently moved to the University of Modena and Reggio Emilia, Modena, Italy. His research interests include simulation, modeling, and characterization of nanoscale CMOS transistors and NVM, with emphasis on hot-carrier effects, quasiballistic transport, Monte Carlo simulation techniques, and with a recent twist toward nanoelectronic (bio) sensors, simulation and characterization of ISFET, and impedance spectroscopy sensors.

Dr. Selmi was a TPC Member of various conferences, including the IEEE International Electron Devices Meeting (IEDM) and the IEEE Symposium on VLSI Technology, and an Editor of IEEE ELECTRON DEVICE LETTERS (EDL).